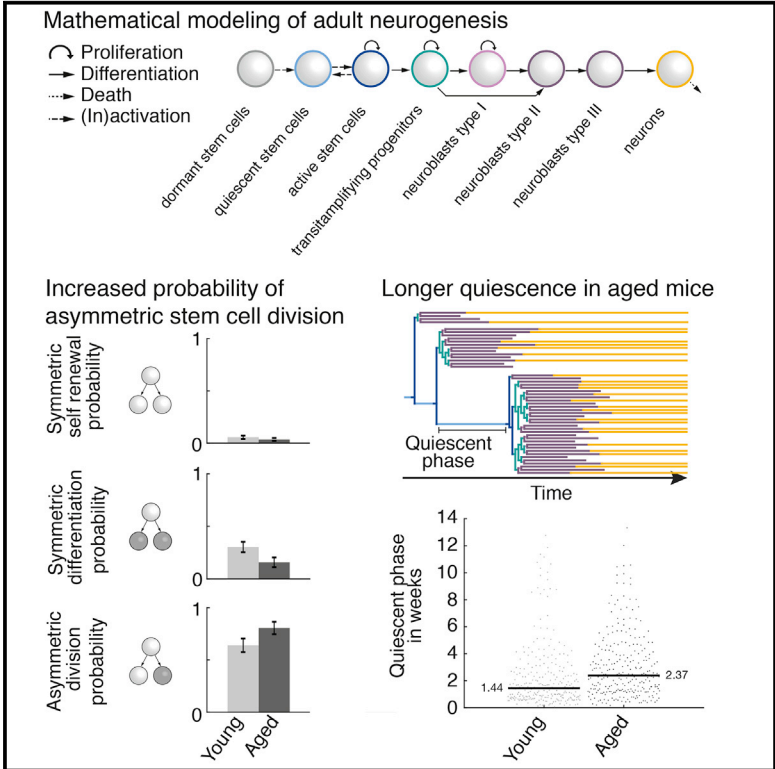


Cell Reports

Increasing Neural Stem Cell Division Asymmetry and Quiescence Are Predicted to Contribute to the Age-Related Decline in Neurogenesis

Graphical Abstract



Authors

Lisa Bast, Filippo Calzolari, Michael K. Strasser, Jan Hasenauer, Fabian J. Theis, Jovica Ninkovic, Carsten Marr

Correspondence

fcalzola@uni-mainz.de (F.C.), ninkovic@helmholtz-muenchen.de (J.N.), carsten.marr@helmholtz-muenchen.de (C.M.)

In Brief

Bast and colleagues traced the lineages of single neural stem cells in the brains of young and aged adult mice to shed light on the age-related decline in neurogenesis. Mathematical modeling of lineage dynamics revealed changes in the behavior of neural stem cells with age.

Highlights

- *In vivo* clonal lineage tracing of adult neural stem cells in aged mice
- Mathematical modeling of adult neurogenesis identifies stem-cell-specific changes
- More frequent asymmetric stem cell divisions and longer quiescence are predicted
- Altered stem cell behavior contributes to the age-related decline in neurogenesis



Increasing Neural Stem Cell Division Asymmetry and Quiescence Are Predicted to Contribute to the Age-Related Decline in Neurogenesis

Lisa Bast,^{1,2,8} Filippo Calzolari,^{3,4,5,8,*} Michael K. Strasser,^{1,7} Jan Hasenauer,^{1,2} Fabian J. Theis,^{1,2} Jovica Ninkovic,^{4,5,6,9,*} and Carsten Marr^{1,9,10,*}

¹Institute of Computational Biology, Helmholtz Zentrum München–German Research Center for Environmental Health, Neuherberg, Germany

²Department of Mathematics, Chair of Mathematical Modeling of Biological Systems, Technische Universität München, Garching, Germany

³Institute for Physiological Chemistry, University Medical Center of the Johannes Gutenberg University Mainz, Mainz, Germany

⁴Institute of Stem Cell Research, Helmholtz Zentrum München–German Research Center for Environmental Health, Neuherberg, Germany

⁵Department of Physiological Genomics, Ludwig-Maximilians University Munich, Munich, Germany

⁶Department for Cell Biology and Anatomy, Biomedical Center of LMU, Ludwig-Maximilians University Munich, Munich, Germany

⁷Present address: Institute for Systems Biology, Seattle, WA, USA

⁸These authors contributed equally

⁹These authors contributed equally

¹⁰Lead Contact

*Correspondence: fcalzola@uni-mainz.de (F.C.), ninkovic@helmholtz-muenchen.de (J.N.), carsten.marr@helmholtz-muenchen.de (C.M.)
<https://doi.org/10.1016/j.celrep.2018.11.088>

SUMMARY

Adult murine neural stem cells (NSCs) generate neurons in drastically declining numbers with age. How cellular dynamics sustain neurogenesis and how alterations with age may result in this decline are unresolved issues. We therefore clonally traced NSC lineages using confetti reporters in young and middle-aged adult mice. To understand the underlying mechanisms, we derived mathematical models that explain observed clonal cell type abundances. The best models consistently show self-renewal of transit-amplifying progenitors and rapid neuroblast cell cycle exit. In middle-aged mice, we identified an increased probability of asymmetric stem cell divisions at the expense of symmetric differentiation, accompanied by an extended persistence of quiescence between activation phases. Our model explains existing longitudinal population data and identifies particular cellular properties underlying adult NSC homeostasis and the aging of this stem cell compartment.

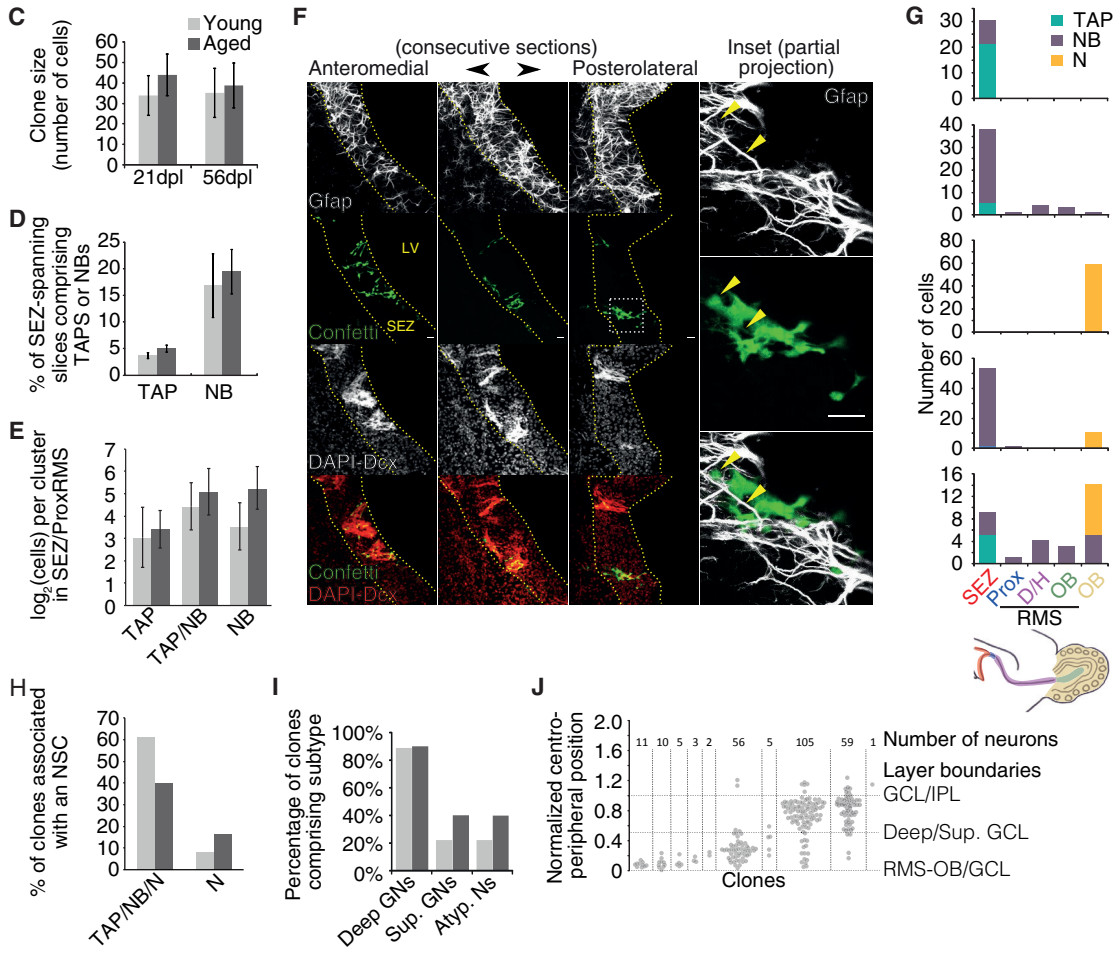
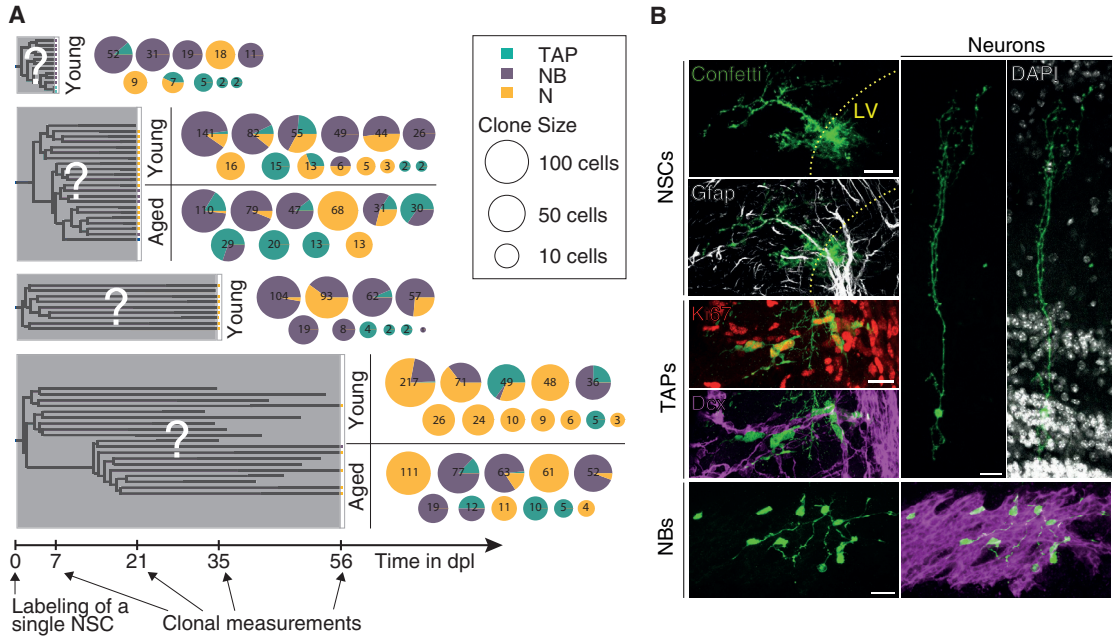
INTRODUCTION

Many adult mammalian somatic tissues are maintained by resident stem and progenitor cell populations and show steep age-dependent functional decline, which positively correlates with reduced cellular turnover (López-Otín et al., 2013). In mice, the generation of new olfactory bulb (OB) interneurons is sustained by subependymal zone (SEZ) adult neural stem cells (NSCs), whose output substantially decreases during aging

(Bouab et al., 2011; Mobley et al., 2013; Molofsky et al., 2006; Piccin et al., 2014). Declining neurogenesis has been associated with changes in local or systemic expression of (or responsiveness to) several factors (Chaker et al., 2015; Daynac et al., 2014; Enwere et al., 2004; Katsimpardi et al., 2014; Lupo et al., 2018; Tropepe et al., 1997). Strikingly, it is still unclear whether the proliferation of NSCs and the migration, differentiation, and survival of their progeny are affected by age *in vivo*. The abundance and proliferative activity of NSCs has been reported as decreasing with age (Enwere et al., 2004) or as being mostly unaffected (Daynac et al., 2014; Tropepe et al., 1997). Different assays employed to evaluate NSC abundance and properties could cause such conflicting interpretations. These comprise *in vitro* assays of cellular behaviors (e.g., neurosphere-forming ability or growth as adherent cultures) known to be significantly affected by exposure to commonly employed mitogens (Codega et al., 2014; Costa et al., 2011) and short-term *ex vivo* analyses of purified cell types (Codega et al., 2014). *In vivo* analyses without clonal lineage tracing (Petreanu and Alvarez-Buylla, 2002) allow for population dynamics snapshots but are limited in the amount of information they can provide on the progeny of single stem cells.

To overcome these limitations, we recently employed *in vivo* clonal lineage tracing to quantitatively describe general features of NSC activity in the SEZ of adult mice at the age of 2 or 3 months (from now on called “young” mice; Calzolari et al., 2015). Our observations support a model of adult OB neurogenesis whereby serial activation of dormant NSCs, followed by a phase of intense neuronal production, is often terminated by NSC exhaustion within a few weeks. Although we posited that this process would gradually erode the dormant NSC pool, explaining the age-associated decline in neurogenic activity, it remained unclear whether and to which extent changes in proliferation and differentiation during lineage progression play a role.





(legend on next page)

RESULTS

In Vivo Clonal Lineage Tracing

To tackle this issue, we performed an *in vivo* clonal lineage tracing analysis of adult murine OB neurogenesis at 12–14 months of age (from now on called “aged” mice). At this age, neurogenesis is already markedly (3- to 4-fold) decreased compared to young adult mice, as reflected by the abundance of immature NSC progeny (Luo et al., 2006) and overall new OB neuron production (Bouab et al., 2011; Molofsky et al., 2006), thus providing a relevant system. We performed *in vivo* clonal lineage tracing using double hemizygous GLAST^{CreERT2}:Confetti transgenic mice (Mori and Tanaka, 2006; Ninkovic et al., 2007), in which NSCs were clonally labeled with a single low dose of tamoxifen (see STAR Methods for details). We chose to analyze clones 21 or 56 days post-labeling (dpl) (Figure 1A) based on our previous observations in young adult mice (analyzed at 7, 21, 35, and 56 dpl; Figure 1A), which had revealed a clear shift in clonal composition across this time window, from immature clones often still containing progenitors at earlier time points to clones composed mostly of mature neurons at 56 dpl (Calzolari et al., 2015). We identified clonal components based on a combination of marker expression, localization, and cell morphology (Figure 1B) in 46 clones from young mice (reported on in Calzolari et al., 2015) and 21 clones from aged mice, in total counting 2,336 single cells. To our surprise, clone size (Figure 1C) and spatial organization (Figure 1D) did not differ between young and aged mice. Similarly to young animals, clones traced in aged mice showed rapid growth, comprising up to 110 cells already at 21 dpl (Figure 1A). The size, composition, and distribution of clusters consisting of transit-amplifying progenitors (TAPs) and neuroblasts (NBs) in the aged SEZ and proximal rostral migratory stream (RMS) suggested multiple doublings as the basis for lineage amplification (Figure 1E), followed by coherent migration of related NBs (Figures 1F, 1G, and S1A). These observations are

similar to the ones in young animals obtained via *in vitro* (Costa et al., 2011) and *in vivo* clonal- (Calzolari et al., 2015) and population-level analyses (Ponti et al., 2013). Moreover, already at 21 dpl, the overall spatial distribution of TAPs, NBs, and neurons was compatible with multiple rounds of NSC activation, resulting in the production of bouts of progeny then coherently undergoing maturation and migration (Figure 1G), similar to observations in young animals (Calzolari et al., 2015). Overall clonal maturation dynamics also resembled those observed in young mice; by 21 dpl, most clones comprised either only progenitor cells (TAPs and NBs) or progenitors and neurons, with only a minority of clones (2/10) consisting of neurons only (Figure 1A). Eight weeks after labeling (56 dpl), the proportion of clones comprising only neurons had increased (4/11), albeit much less than in young animals, where 7 out of 12 clones consist of only neurons (Figure 1A). These clones were rarely found in association (i.e., in the same hemisphere) with a radial astrocyte (Figure 1H), suggestive of NSC exhaustion being the major mechanism of termination of NSC-derived OB neurogenesis, like in the young SEZ (Calzolari et al., 2015). Finally, the inter- and intra-clonal diversity and distribution of mature neurons in the OB also indicated consistency with the principles deduced from observations in young animals (Calzolari et al., 2015; Merkle et al., 2014), with mostly subtype-biased, restricted clonal neurogenic activity (Figures 1I, 1J, and S1B–S1F). These observations revealed that individual NSC clones active in the aged SEZ show no signs of grossly impaired neurogenic activity. This raised the possibility that subtle changes in clonal dynamics may contribute to the known decline in overall neurogenic output from the aged SEZ.

A Stochastic Population Model of Adult Neurogenesis

In order to define quantitative aspects of neurogenic lineage progression and to compare competing hypotheses of clonal dynamics, we mathematically modeled adult neurogenesis at

Figure 1. *In Vivo* Clonal Measurements of NSCs in the SEZ of Young and Aged Mice

- (A) Experimental design. The clonal progeny of a single labeled NSC is observed at one of four different time points (7, 21, 35, and 56 days post-labeling [dpl]) in young and aged mice. The progeny is classified into four cell types: NSC; transit-amplifying progenitor (TAP); neuroblast (NB); and neuron (N), of which, however, only the latter three are reported in the pie charts, indicating the number and composition of clones observed at each time point.
- (B) Examples of cells at distinct stages of neurogenic lineage progression, as labeled in *Glax1^{CreERT2}:Confetti* mice. Markers were used to positively identify cell states via GFAP (NSCs) and *Dcx* (NBs) expression. TAPs and Ns were defined by a combination of lack of marker expression, localization, and morphology. The proliferation marker *Ki67* is shown to confirm the TAP identity of SEZ-localized *Dcx*-negative cells but was not regularly used to identify cells. Dashed line highlights the LV border. Scale bars 20 μ m.
- (C) Average clone sizes at 21 and 56 dpl for young and aged mice. We show mean \pm SEM ($n = 14$ and 12 in young and $n = 12$ and 11 in aged mice, respectively).
- (D) Clonal average percentage of SEZ-encompassing sagittal sections comprising TAPs or NBs, revealing broader distribution for NBs than TAPs, a feature not affected by age. Error bars represent SEM.
- (E) Average size of cell clusters of the indicated compositions, as found in the SEZ and proximal RMS of young and aged mice. Error bars represent SEM.
- (F) Example of subclonal expansion, showing clone components (Confetti reporter, green) distributed across three consecutive SEZ sections in a 1-year-old brain. Insets to the right focus on the most posterolateral section, where a single GFAP-positive cell is surrounded by clonally related cells (max-intensity projection of a reduced number of optical sections to better highlight Confetti/GFAP colocalization). Yellow arrowheads point to GFAP signal in the soma and radial process. Dashed curves indicate SEZ borders; dashed box highlights the inset. LV, lateral ventricle. Scale bars 20 μ m.
- (G) Five exemplary aged clones showing numbers of cells per cell stage (color code) along the rostral migratory stream (RMS) SEZ-to-OB axis, based on binning as indicated in the scheme at the bottom of the panel, depicting a partial sagittal mouse brain section. RMS is subdivided in proximal (Prox), descending horizontal limbs (D/H), and RMS-OB (OB). Ocr OB refers to OB locations external to the RMS-OB. Individual clones were sampled at 21, 21, 56, 56, and 21 dpl, from the top.
- (H) Percentage of clones, either comprising both progenitors and neurons (TAP, NB, N) or only neurons (N), for which a radial astrocyte sharing the clone's Confetti label could be found in the ipsilateral SEZ. Importantly, this does not imply physical association between radial astrocyte and differentiating cells.
- (I) Percentage of clones comprising the indicated OB neuronal subtypes, for both young and aged mice. Data for young mice are from Calzolari et al. (2015).
- (J) Normalized position of all neurons found in aged mice, subdivided by clone, with number of neurons per clone indicated above the graph.

young and middle ages with a stochastic population model (see STAR Methods for details) using our clonal data and a limited set of published population-level data, as previously done for other systems (Chabab et al., 2016; Flossdorf et al., 2015; Yang et al., 2015).

Murine NSCs interconvert between actively proliferating, progeny-producing, and temporarily quiescent states (Basak et al., 2012, 2018; Costa et al., 2011; Giachino et al., 2014). Dormancy is a recognized feature of the majority of (young adult) NSCs (Urbán et al., 2016), possibly since late embryonic times (Falk et al., 2017; Fuentealba et al., 2015; Furutachi et al., 2015). We thus modeled the adult neurogenic lineage as comprising three NSC states (fully “dormant” [dS], “quiescent” [qS], and “active,” proliferating [aS]), transit-amplifying progenitors (TAPs), proliferating (NB I) and non-proliferating (NB II/III) neuroblasts, and neurons (N) (see Figure 2A and STAR Methods for details on model construction). We relied on published data only to fix the dormant NSC activation rate and to constrain the (in)activation rates for the remaining NSC states (Figure S2A), respectively (Shook et al., 2012). By defining activation and inactivation, proliferation, migration rates, the proportion of initially labeled stem cells as dS, qS, or aS, and the proportion of surviving NBs as unknown parameters, we set up stochastic reaction rate equations that model clonal dynamics. For each of the three proliferating states (aS, TAP, and NB I), we allowed for four different division modes: asymmetric (A); symmetric (S); constrained (C), where the proportion of symmetric and asymmetric divisions is regulated by a single parameter p_d ; and unconstrained (U), where any combination of asymmetric division, self-renewal, and symmetric differentiation probabilities is allowed (see Figures 2A–2C and STAR Methods for details). We here define an asymmetric division as a cell division followed by the transition of only one daughter cell to the next stage in our model (Figures 2A and 2B) before it possibly divides again. The other daughter cell initially persists in the “parental” cell state, to later divide again or undergo transitions as allowed by the model (e.g., in the case of an aS, to return to a quiescent qS state). It should be noted that, although our model directly couples certain cell state transitions to cell division (Figure 2B), some of these cell fate choices may in reality also happen sometime after the cell has divided. Our approach allows exploration of a very diverse set of proliferative behaviors. Combining the four different division modes across three proliferative compartments results in $4^3 = 64$ different possible models (Figure 2C) with a varying number of parameters and complexity. Unknown model parameters were estimated for each model separately by fitting means, variances, and covariances of modeled TAPs, NBs, and Ns to the respective moments of the measured clonal compositions (exemplarily shown in Figure S2B) using maximum-likelihood estimation (Buchholz et al., 2013). Parameter boundaries and constraints were carefully chosen in accordance with prior knowledge (see STAR Methods and Table S2). The 64 different models were compared according to the Bayesian Information Criterion (BIC), a score that ranks models based on both their complexity and their ability to explain the observed data (Figure 2D). The five best performing models (Figure 2D) indicate that changes in the division mode of active NSCs are required to explain the observed clonal dynamics. Although in young mice symmetric stem cell divisions (allowed by S, C, and U division modes) are required, asymmetric

(A) stem cell divisions (the simplest division mode with only one parameter) suffice to explain clonal measurements in aged mice (Figure 2D; Table S3) in the top five models.

However, comparison of the best-ranking models did not reveal any model that clearly outperforms the others. Instead, differences in the Bayesian information criterion (BIC) values for the top ten models describing clonal dynamics at 2 and 14 months were below 4 (Figure 2E), which are not considered decisive (Kass and Raftery, 1995). Therefore, we derived average models for young and aged mice by weighting the resulting parameter estimates with the posterior probability of the model (BIC weight; see STAR Methods and Figure 2F) to yield robust predictions.

Based on the weighted average proportion of symmetric self-renewal, symmetric differentiation, and asymmetric division (Figure 2G), we still find that asymmetric stem cell divisions are more prevalent in aged compared to young mice ($80.6\% \pm 5.8\%$ versus $64.0\% \pm 6.5\%$ in young mice; mean \pm SEM of weighted posterior probabilities), and symmetric differentiation decreases from $30.4\% \pm 5.0\%$ in young mice to $15.9\% \pm 4.7\%$ in aged mice. This result still holds if we only consider the data points at 21 and 56 dpl for young mice, highlighting its robustness (Figure S2D). Our models also identify a high, age-independent percentage of symmetric self-renewal of TAPs ($25.9\% \pm 2.9\%$ in young; $18.2\% \pm 2.7\%$ in aged mice) and rapid differentiation of NBs, two properties that are consistent with existing knowledge about these cell types (Ponti et al., 2013). Interestingly, aging seems to specifically affect NSC behavior, but at several levels, as we also observe a substantial decrease in the transition rates between active and quiescent NSCs, such that both activation and inactivation occur less frequently in aged mice (Figure 2H).

Model Validation

To evaluate the average model for young mice, we compared its predictions to independent population-level data (Shook et al., 2012) on the temporal evolution of cell type abundances during aging. We observed a very good agreement between model and measurements for TAPs and NBs (Figure 3A), which suggests that our clonal labeling approach was not biased toward a functionally distinct subset of NSCs. An adaptation of the average parameters from young to aged mice (using Hill kinetics; see STAR Methods for details and Figure S3) to explicitly consider a temporal shift in NSC behavior leads to an age-dependent model that describes the decrease of TAPs and NBs similarly well (Figure 3A). For further validation, we compared measured clone size (Figure 3B) and cell type composition (Figure 3C) with our model and found very good agreement. Lastly, we tested whether our model can explain the observed change in the fraction of neuron-only clones with age (see Figures 1A and 3D). We found that our young and aged models correctly describe the shift toward less neuron-only clones with age and reject the hypothesis that the observed percentage of neuron-only clones in aged animals ($4/11 = 36\%$) can be explained by the young model with a p value of 0.015.

Overall, these validation steps suggest that our model reliably captures quantitative aspects of adult OB neurogenesis. We thus employed it to explore quantitative aspects of adult neurogenic lineage progression.

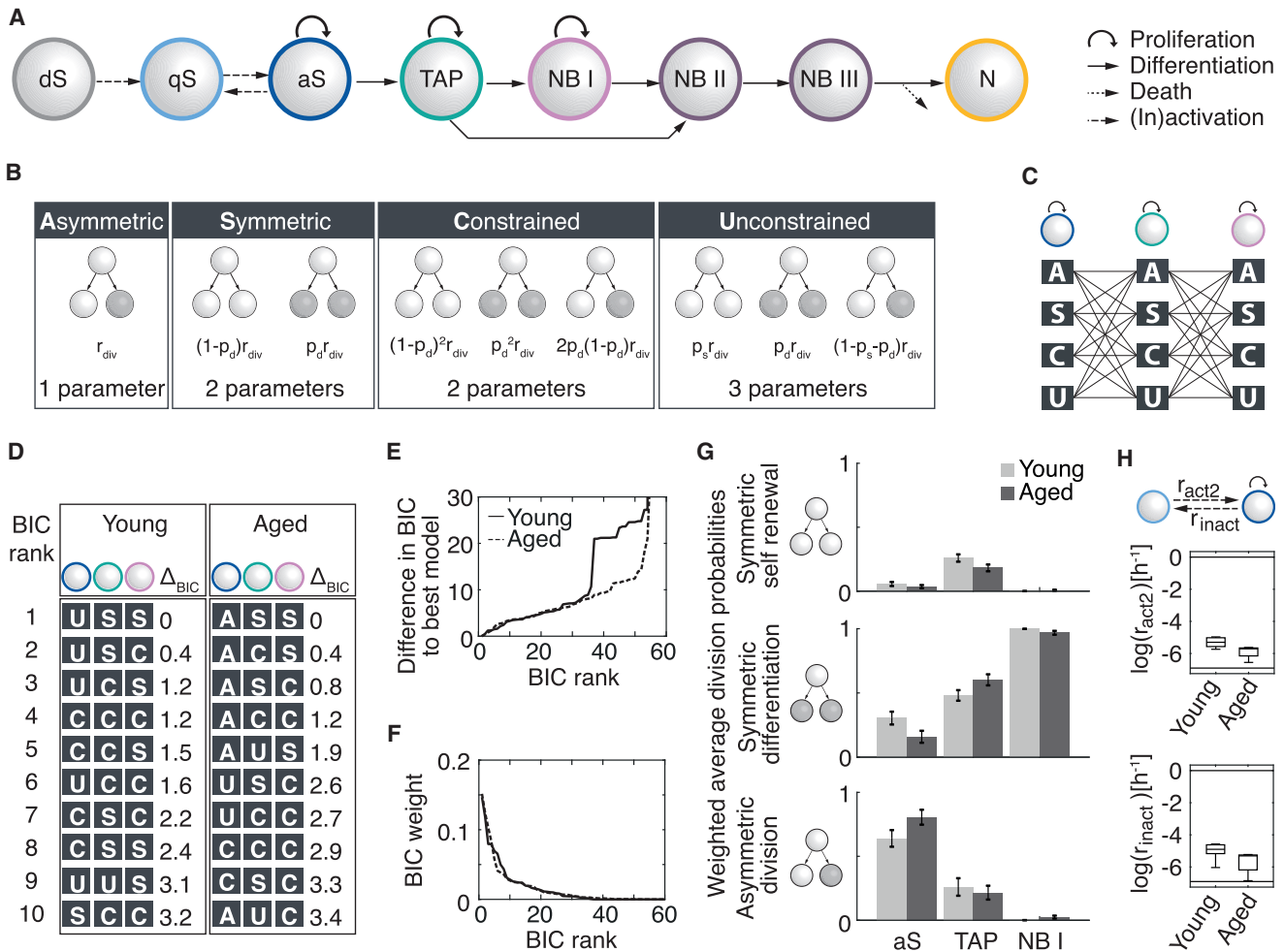


Figure 2. A Population Model Fits Clonal Data with Increased Asymmetric Stem Cell Divisions and Longer Activation and Inactivation Times in Aged Mice

(A) Adult neurogenesis model: the pool of dormant stem cells (dS) is depleted over time. Cells can then be activated and inactivated by switching between the quiescent (qS) and active (aS) state. Active stem cells (aS), transit-amplifying progenitors (TAPs), and neuroblasts of type I (NB I) divide. Neuroblasts of type II (NB II) no longer divide and migrate along the SEZ to the olfactory bulb, where they eventually become neuroblasts of type III, which are either depleted via cell death or become neurons (N).

(B) Division modes for dividing cell types: asymmetric divisions (A) give rise to a daughter cell of the same type and a daughter cell of the subsequent type, symmetric divisions (S) produce two daughters of the same cell type, constrained divisions (C) assume independent differentiation between sister cells, and the unconstrained division (U) is the most flexible mode. The number of model parameters increases from left to right with equal model complexity for modes S and C.

(C) Combinations of the four division modes for dividing aS, TAP, and NB I lead to 64 different models.

(D) The 64 different models are fitted separately to the clonal data from young and aged mice and compared via the Bayesian information criterion (BIC). Asymmetric stem cell divisions are prevalent in the top five models for aged mice.

(E) BIC differences for all 64 models to the best model for young (solid line) and aged (dashed line) mice.

(F) Estimated posterior model probability (BIC weight) for young (solid line) and aged (dashed line) mice indicate that the top ten models dominate.

(G) Division probabilities calculated from all 64 models as a weighted average according to their BIC weights for young (light gray) and aged (dark gray) mice show strong TAP self-renewal (top), rapid NB differentiation (middle), and increased asymmetric stem cell divisions in aged mice (bottom). Error bars indicate \pm SE of the weighted mean (SEM_w).

(H) Weighted boxplots show the decrease with age in the weighted probability distribution for log-transformed (in)activation rates resulting from 64 models for young (left) and aged (right). Boxes depict the 1st, 2nd, and 3rd quartiles. Horizontal lines at top and bottom represent parameter boundaries, which were carefully chosen according to biological plausibility (see Table S2).

Model-Based Predictions of Lineage Progression

To investigate the impact of the identified changes during aging at the clonal level, we generated single-cell genealogies from the young and aged model (see STAR Methods for details). Specif-

ically, we simulated 1,000 clones for young and aged mice (see Figure 4A for five exemplary genealogies) using the inferred weighted average parameters (Figures 2G, 2H, and S2C) and calculated genealogical metrics (Figure 4B) to compare (sub)

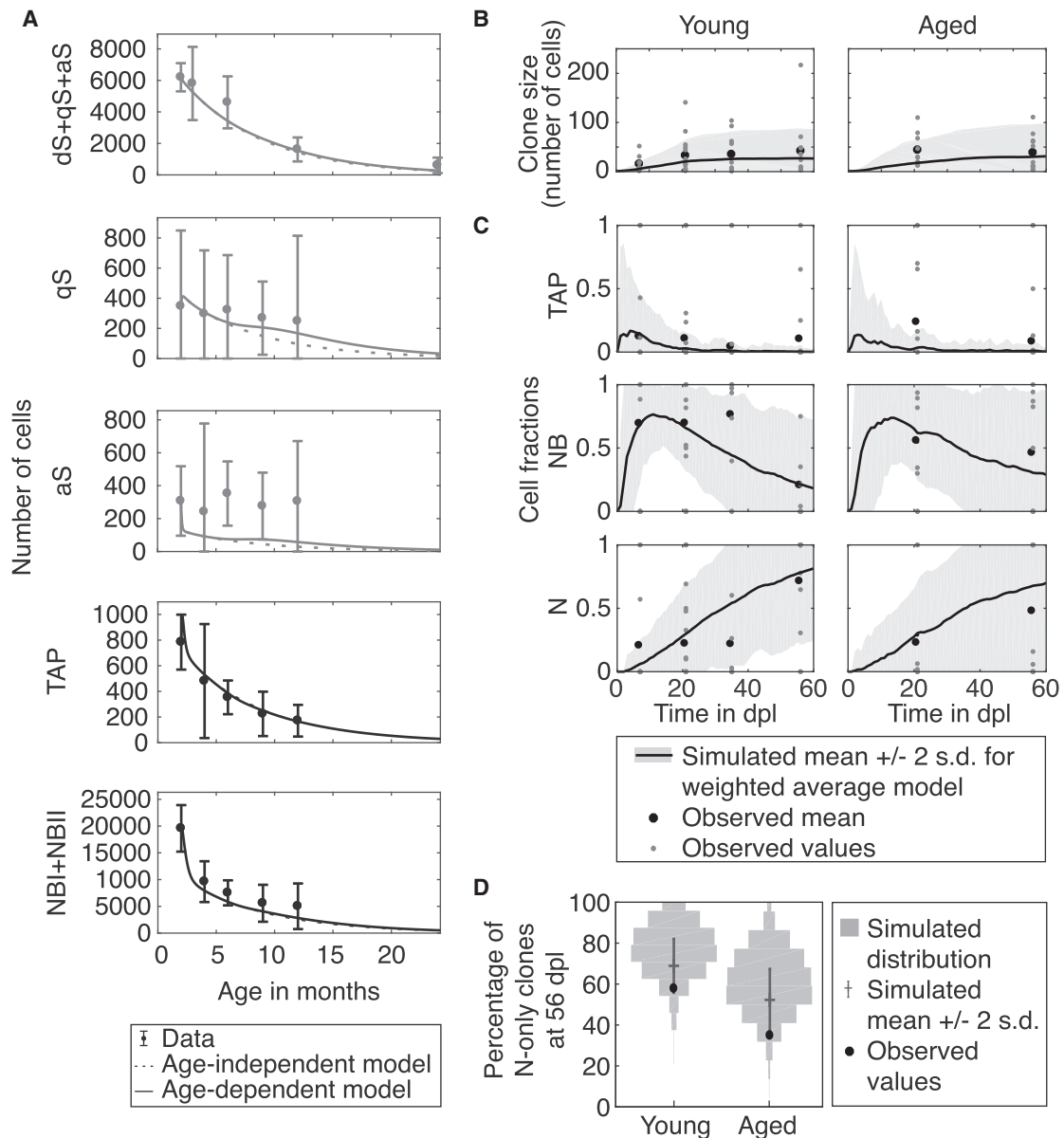


Figure 3. Clonal and Population Level Data Validate Weighted Average Models

(A) Predicted TAP and NB cell numbers of age-dependent and age-independent (solid and dashed lines) weighted average models agree with population data from Daynac et al. (2016); (mean \pm 2 SD; $n \geq 4$ per time point). Initial conditions are set to earliest observed measurement of the respective cell type. Models include halfway migration of neuroblasts to be consistent with the population study data, which are the number of cells obtained after dissociating the lateral wall of the lateral ventricles, thus accessing only a portion of the whole NB population. Stem cell numbers (gray dots with error bars) were used to constrain (in) activation rate parameters (Figure S2A).

(B) Clone size in average models (solid lines) agree with observed cell numbers (small gray dots) and their mean (large black dots). Model variability is calculated from 500 SSA simulations (gray shaded area; ± 2 SD errors).

(C) Average models accurately predict cell fractions over time.

(D) Average models correctly predict the decline of neuron-only clones with age. Number of neuron-only clones calculated from model simulations (gray distribution plot) compared to observed values (black dots) is shown.

clonal dynamics during aging. We define a subclone as that part of a clone that emerges from a recently activated NSC and is separated from the rest of the clone by a phase of quiescence (see Figure 4B). We found that the inferred age-related changes

in NSC behavior impacted simulated clonal dynamics at two levels: the increased probability of asymmetric aS divisions, which occurs at the expense of symmetric differentiation divisions (Figure 2G), prolongs the aS expansion phase of subclones

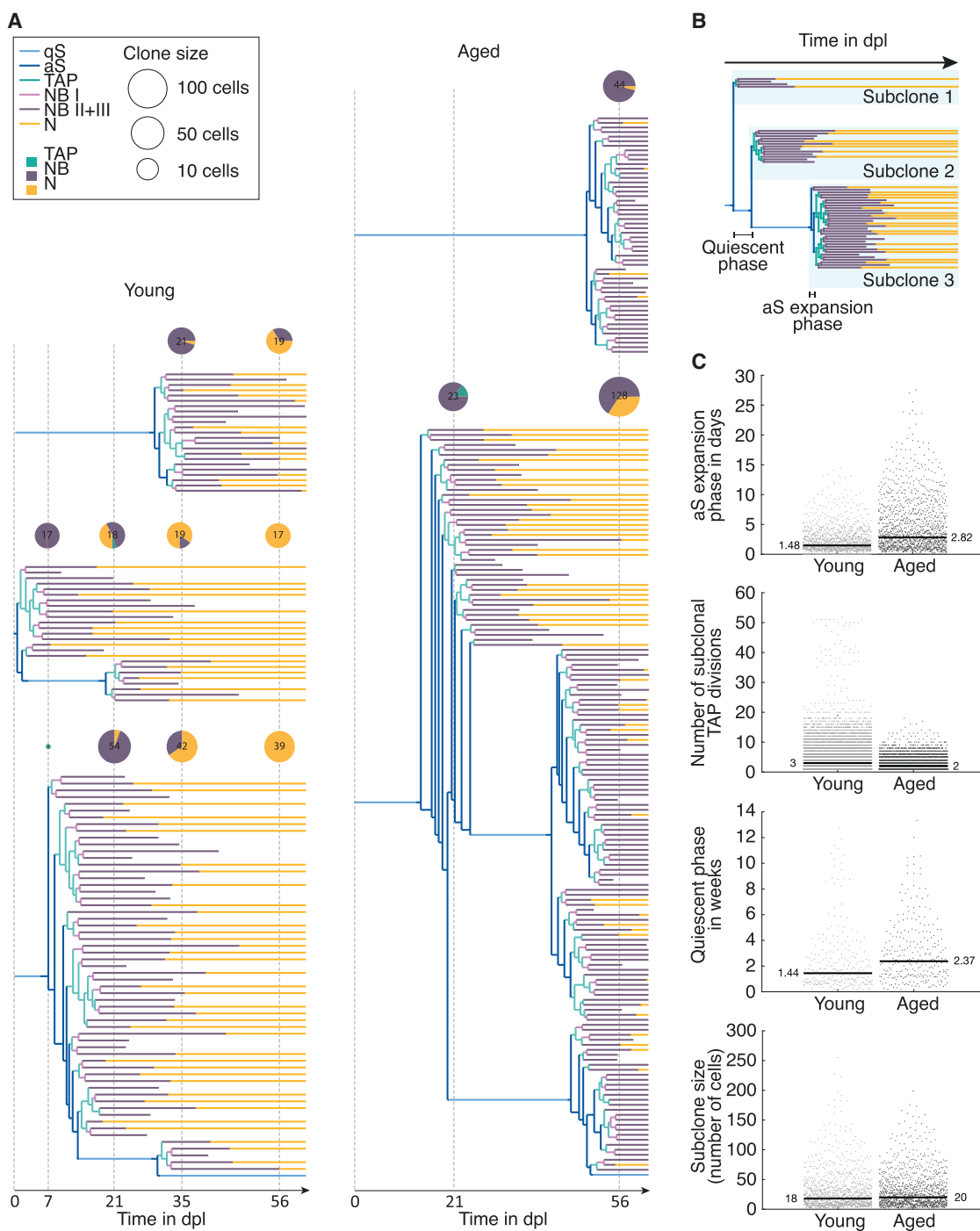


Figure 4. Lineage Tree Simulations Predict Longer Quiescent and aS Expansion Phases in Aged Mice

(A) Five exemplary simulated lineage trees from the young (left) and aged (right) model. Pie charts indicate clone size and composition (number of TAPs, NBs, and Ns) at the experimental time points to allow a comparison with the experimental data shown in Figure 1A.

(B) Definition of genealogical metrics.

(C) Predicted differences between young and aged neurogenesis calculated from 1,000 simulated lineage trees from the average young and aged model. Medians are shown as a black line.

but is thwarted by the lowered NSC activation and inactivation rates, which result in increased NSC quiescence and the less frequent generation of subclones (Figure 4C). Interestingly, the subclone size is only slightly increased with age, as the increased aS expansion phase is counterbalanced by the reduction in the number of TAP divisions (Figures 4A and 4C). It is thus tempting to speculate that the inferred “pro-neurogenic” (i.e., NSC exhaustion-delaying) changes in these parameters may reflect a mechanism to compensate for age-associated neurogenesis-depleting processes. Increasing the probability of asymmetric aS divisions and extending the phase of NSC quiescence both reduce the rate at which the NSC population erodes by extending the time between the initial qS activation and the eventual exhaustion of active lineages. Clearly, though, these same processes also dampen the clonal output, suggesting that a trade-off between competing pressures may be shaping the temporal profile of adult neurogenesis.

DISCUSSION

According to our analysis, the observed decline in neuronal output is mainly influenced by the depletion of the dormant NSC pool but also by changes in the frequency and mode of NSC divisions. Specifically, clonal data, modeling, and validation steps provide evidence for asymmetry and quiescence being core and age-modulated features of adult NSC behavior. Interestingly, *in vivo* imaging of adult NSCs in the hippocampal dentate gyrus recently provided direct evidence for asymmetric adult NSC divisions (Pilz et al., 2018), and the interconversion between actively proliferating and quiescent NSC states is well appreciated (Basak et al., 2012; Giachino et al., 2014).

A recent report addressing NSC behavior in the juvenile and young adult mouse SEZ came, however, to strikingly different conclusions from the ones we reached (Obernier et al., 2018). Obernier and colleagues performed *in vivo* clonal lineage tracing of active NSCs, with a limited focus on their immediate progeny (i.e., TAPs), observing almost exclusively clones consisting of either small numbers of radial astrocytes or clusters of GFAP[−]/Ascl1⁺ cells. The relative abundance of such clusters (20%–30% and 70%–80%, respectively) was suggested to reflect the probabilities of symmetric self-renewing and differentiative NSC divisions. Importantly, our own data support the view that radial astrocyte-like cells in physical association with TAP clusters are a rare observation, and this co-occurrence in any case would not necessarily imply asymmetric NSC divisions. However, several considerations and lines of evidence provide support for the scenario we put forward: (1) a significant proportion of actively dividing NSCs has been shown to be Ascl1⁺ in all main adult neurogenic populations (Kim et al., 2011; Ponti et al., 2013; Urbán et al., 2016) and (2) GFAP expression is absent from at least some actively proliferating SEZ NSCs (Giachino et al., 2014), indicating that commonly employed sets of markers can be critically ambiguous at this specific lineage transition phase. This issue clearly also applies to the identification approach we took, which, however, is much more robust to individual misclassification events, because it relies on means and (co)variances of cell numbers rather than on binary cluster classifications (see Figures S2D and S2E and STAR Methods for details). Importantly,

the NSC division mode proposed by Obernier et al. failed to explain the authors’ own data describing the age-related decline in adult neurogenesis, compelling the authors to introduce a modified model. This requires so-called B2 astrocytes (also referred to in the literature as “niche astrocytes”; Chaker et al., 2015) to *en masse* behave as symmetrically dividing and committedly neurogenic NSCs, properties for which there is no evidence. Interestingly, although our modeling results lend only relatively weak support to strictly symmetric models (ranked only as 10th best model and worse in young; 18th and worse in aged mice), the corresponding NSC division probabilities intriguingly match those suggested by Obernier and colleagues (see red highlights in Table S3). To reconcile the currently discrepant views of NSC behavior, we suggest the existence of transient, morphologically TAP-like active NSCs (i.e., unipolar, clonally clustered, and located in subventricular positions), possessing the ability to regain a typical NSC morphology and return to quiescence. Although evidence for the existence of such cell stage is currently lacking, existing or novel tools may allow testing this prediction.

In conclusion, we have performed the first *in vivo* clonal analysis of neural stem cell behavior in aged mammals and mathematically modeled adult neurogenesis to define quantitative aspects of lineage transition in young and aged mice. Despite only minor differences between the two clonal datasets, our model fits the observed data and unveils changes in a restricted set of key parameters. These parameters lead to relatively subtle alterations in clonal dynamics, which, however, explain the observed stronger tendency of young animals to produce mature clones and are in agreement with the drastic population-level age-related decline in adult OB neurogenesis.

STAR★METHODS

Detailed methods are provided in the online version of this paper and include the following:

- KEY RESOURCES TABLE
- CONTACT FOR REAGENT AND RESOURCE SHARING
- EXPERIMENTAL MODEL AND SUBJECT DETAILS
 - Animal handling, breeding and Tamoxifen administration scheme
 - Mouse lines
- METHOD DETAILS
 - 1. Experimental methods
 - 2. Computational methods
- QUANTIFICATION AND STATISTICAL ANALYSIS
- DATA AND SOFTWARE AVAILABILITY

SUPPLEMENTAL INFORMATION

Supplemental Information includes four figures and four tables and can be found with this article online at <https://doi.org/10.1016/j.celrep.2018.11.088>.

ACKNOWLEDGMENTS

We thank M. Goetz (LMU Munich and Helmholtz Zentrum München) for comments on an early version of the manuscript and A. Kazeroonian (TU Munich) and C. Loos (Helmholtz Zentrum München) for computational support. L.B.

was supported by the German Research Foundation (DFG) within the Collaborative Research Centre CRC1243, Subproject A17. F.C. was supported in part by NEURON-ERANET (01EW1604) and DFG (CRC1080) grants to Dr. Benedikt Berninger (UMC Mainz) and by the Inneruniversitäre Forschungsförderung of the University Medical Center of Johannes Gutenberg University Mainz.

AUTHOR CONTRIBUTIONS

F.C. generated data. L.B. and F.C. analyzed data. L.B. constructed model with F.C. and C.M. L.B. performed parameter inference and model simulations with C.M. and M.S. and advice from J.H. and F.T. F.C. and J.N. initiated the project with F.T. J.N. and C.M. supervised the study. L.B., F.C., J.N., and C.M. wrote the paper.

DECLARATION OF INTERESTS

The authors declare no competing interests.

Received: December 4, 2017

Revised: July 31, 2018

Accepted: November 21, 2018

Published: December 18, 2018

REFERENCES

- Basak, O., Giachino, C., Fiorini, E., Macdonald, H.R., and Taylor, V. (2012). Neurogenic subventricular zone stem/progenitor cells are Notch1-dependent in their active but not quiescent state. *J. Neurosci.* *32*, 5654–5666.
- Basak, O., Krieger, T.G., Muraro, M.J., Wiebrands, K., Stange, D.E., Frias-Aldeguer, J., Rivron, N.C., van de Wetering, M., van Es, J.H., van Oudenaarden, A., et al. (2018). *Troy+* brain stem cells cycle through quiescence and regulate their number by sensing niche occupancy. *Proc. Natl. Acad. Sci. USA* *115*, E610–E619.
- Bhat, H., and Kumar, N. (2010). On the derivation of the Bayesian Information Criterion. <http://citeseerx.ist.psu.edu/viewdoc/download?doi=10.1.1.723.8015&rep=rep1&type=pdf>.
- Bouab, M., Paliouras, G.N., Aumont, A., Forest-Bérard, K., and Fernandes, K.J.L. (2011). Aging of the subventricular zone neural stem cell niche: evidence for quiescence-associated changes between early and mid-adulthood. *Neuroscience* *173*, 135–149.
- Boyd, S., and Vandenberghe, L. (2016). *Convex Optimization* South Asia Edition (Cambridge University).
- Buchholz, V.R., Flossdorf, M., Hensel, I., Kretschmer, L., Weissbrich, B., Gräf, P., Verschoor, A., Schiemann, M., Höfer, T., and Busch, D.H. (2013). Disparate individual fates compose robust CD8+ T cell immunity. *Science* *340*, 630–635.
- Calzolari, F., Michel, J., Baumgart, E.V., Theis, F., Götz, M., and Ninkovic, J. (2015). Fast clonal expansion and limited neural stem cell self-renewal in the adult subependymal zone. *Nat. Neurosci.* *18*, 490–492.
- Chabab, S., Lescroart, F., Rulands, S., Mathiah, N., Simons, B.D., and Blanpain, C. (2016). Uncovering the number and clonal dynamics of *Mesp1* progenitors during heart morphogenesis. *Cell Rep.* *14*, 1–10.
- Chaker, Z., Aïd, S., Berry, H., and Holzenberger, M. (2015). Suppression of IGF-I signals in neural stem cells enhances neurogenesis and olfactory function during aging. *Aging Cell* *14*, 847–856.
- Cochran, W.G. (2007). *Sampling Techniques*, 3rd Edition (John Wiley & Sons).
- Codega, P., Silva-Vargas, V., Paul, A., Maldonado-Soto, A.R., Deleo, A.M., Pastrana, E., and Doetsch, F. (2014). Prospective identification and purification of quiescent adult neural stem cells from their in vivo niche. *Neuron* *82*, 545–559.
- Costa, M.R., Ortega, F., Brill, M.S., Beckervordersandforth, R., Petrone, C., Schroeder, T., Götz, M., and Berninger, B. (2011). Continuous live imaging of adult neural stem cell division and lineage progression in vitro. *Development* *138*, 1057–1068.
- Daynac, M., Pineda, J.R., Chicheportiche, A., Gauthier, L.R., Morizur, L., Boussin, F.D., and Mouchon, M.-A. (2014). TGF β lengthens the G1 phase of stem cells in aged mouse brain. *Stem Cells* *32*, 3257–3265.
- Daynac, M., Morizur, L., Chicheportiche, A., Mouchon, M.-A., and Boussin, F.D. (2016). Age-related neurogenesis decline in the subventricular zone is associated with specific cell cycle regulation changes in activated neural stem cells. *Sci. Rep.* *6*, 21505.
- Eliás, J., and Vořechovský, M. (2016). Modification of the Audze–Eglajs criterion to achieve a uniform distribution of sampling points. *Adv. Eng. Softw.* *100*, 82–96.
- Engblom, S. (2006). Computing the moments of high dimensional solutions of the master equation. *Appl. Math. Comput.* *180*, 498–515.
- Enwere, E., Shingo, T., Gregg, C., Fujikawa, H., Ohta, S., and Weiss, S. (2004). Aging results in reduced epidermal growth factor receptor signaling, diminished olfactory neurogenesis, and deficits in fine olfactory discrimination. *J. Neurosci.* *24*, 8354–8365.
- Falk, S., Bugeon, S., Ninkovic, J., Pilz, G.-A., Postiglione, M.P., Cremer, H., Knoblich, J.A., and Götz, M. (2017). Time-specific effects of spindle positioning on embryonic progenitor pool composition and adult neural stem cell seeding. *Neuron* *93*, 777–791.e3.
- Flossdorf, M., Rössler, J., Buchholz, V.R., Busch, D.H., and Höfer, T. (2015). CD8+ T cell diversification by asymmetric cell division. *Nat. Immunol.* *16*, 891–893.
- Fröhlich, F., Thomas, P., Kazeroonian, A., Theis, F.J., Grima, R., and Hasenauer, J. (2016). Inference for stochastic chemical kinetics using moment equations and system size expansion. *PLoS Comput. Biol.* *12*, e1005030.
- Fröhlich, F., Kaltenbacher, B., Theis, F.J., and Hasenauer, J. (2017). Scalable parameter estimation for genome-scale biochemical reaction networks. *PLoS Comput. Biol.* *13*, e1005331.
- Fuentealba, L.C., Rompani, S.B., Parraguez, J.I., Obernier, K., Romero, R., Cepco, C.L., and Alvarez-Buylla, A. (2015). Embryonic origin of postnatal neural stem cells. *Cell* *161*, 1644–1655.
- Furutachi, S., Miya, H., Watanabe, T., Kawai, H., Yamasaki, N., Harada, Y., Imayoshi, I., Nelson, M., Nakayama, K.I., Hirabayashi, Y., and Gotoh, Y. (2015). Slowly dividing neural progenitors are an embryonic origin of adult neural stem cells. *Nat. Neurosci.* *18*, 657–665.
- Gardiner, C. (2010). *Stochastic Methods: A Handbook for the Natural and Social Sciences* (Springer).
- Gatz, D.F., and Smith, L. (1995). The standard error of a weighted mean concentration—II. Estimating confidence intervals. *Atmos. Environ.* *29*, 1195–1200.
- Giachino, C., Basak, O., Lugert, S., Knuckles, P., Obernier, K., Fiorelli, R., Frank, S., Raineteau, O., Alvarez-Buylla, A., and Taylor, V. (2014). Molecular diversity subdivides the adult forebrain neural stem cell population. *Stem Cells* *32*, 70–84.
- Gillespie, D.T. (1992). A rigorous derivation of the chemical master equation. *Physica A* *188*, 404–425.
- Gillespie, D.T. (2001). Approximate accelerated stochastic simulation of chemically reacting systems. *J. Chem. Phys.* *115*, 1716–1733.
- Kass, R.E., and Raftery, A.E. (1995). Bayes factors. *J. Am. Stat. Assoc.* *90*, 773–795.
- Katsimpardi, L., Litterman, N.K., Schein, P.A., Miller, C.M., Loffredo, F.S., Wojtkiewicz, G.R., Chen, J.W., Lee, R.T., Wagers, A.J., and Rubin, L.L. (2014). Vascular and neurogenic rejuvenation of the aging mouse brain by young systemic factors. *Science* *344*, 630–634.
- Kazeroonian, A., Fröhlich, F., Raue, A., Theis, F.J., and Hasenauer, J. (2016). CERENA: chemical reaction network analyzer—a toolbox for the simulation and analysis of stochastic chemical kinetics. *PLoS ONE* *11*, e0146732.
- Kim, E.J., Ables, J.L., Dickel, L.K., Eisch, A.J., and Johnson, J.E. (2011). *Ascl1* (*Mash1*) defines cells with long-term neurogenic potential in subgranular and subventricular zones in adult mouse brain. *PLoS ONE* *6*, e18472.

- Klein, A.M., and Simons, B.D. (2011). Universal patterns of stem cell fate in cycling adult tissues. *Development* 138, 3103–3111.
- Link, W.A., and Barker, R.J. (2006). Model weights and the foundations of multimodel inference. *Ecology* 87, 2626–2635.
- López-Otin, C., Blasco, M.A., Partridge, L., Serrano, M., and Kroemer, G. (2013). The hallmarks of aging. *Cell* 153, 1194–1217.
- Luo, J., Daniels, S.B., Lenington, J.B., Notti, R.Q., and Conover, J.C. (2006). The aging neurogenic subventricular zone. *Aging Cell* 5, 139–152.
- Lupo, G., Nisi, P.S., Esteve, P., Paul, Y.-L., Novo, C.L., Sidders, B., Khan, M.A., Biagioni, S., Liu, H.-K., Bovolenta, P., et al. (2018). Molecular profiling of aged neural progenitors identifies Dbx2 as a candidate regulator of age-associated neurogenic decline. *Aging Cell* 17, e12745.
- Merkle, F.T., Fuentealba, L.C., Sanders, T.A., Magno, L., Kessaris, N., and Alvarez-Buylla, A. (2014). Adult neural stem cells in distinct microdomains generate previously unknown interneuron types. *Nat. Neurosci.* 17, 207–214.
- Mobley, A.S., Bryant, A.K., Richard, M.B., Brann, J.H., Firestein, S.J., and Greer, C.A. (2013). Age-dependent regional changes in the rostral migratory stream. *Neurobiol. Aging* 34, 1873–1881.
- Molofsky, A.V., Slutsky, S.G., Joseph, N.M., He, S., Pardal, R., Krishnamurthy, J., Sharpless, N.E., and Morrison, S.J. (2006). Increasing p16INK4a expression decreases forebrain progenitors and neurogenesis during ageing. *Nature* 443, 448–452.
- Mori, T., and Tanaka, T. (2006). Effect of transition metal doping and carbon doping on thermoelectric properties of YB₆₆ single crystals. *J. Solid State Chem.* 179, 2889–2894.
- Ninkovic, J., Mori, T., and Götz, M. (2007). Distinct modes of neuron addition in adult mouse neurogenesis. *J. Neurosci.* 27, 10906–10911.
- Obernier, K., Cebrian-Silla, A., Thomson, M., Parraguez, J.I., Anderson, R., Guinto, C., Rodas Rodriguez, J., Garcia-Verdugo, J.-M., and Alvarez-Buylla, A. (2018). Adult neurogenesis is sustained by symmetric self-renewal and differentiation. *Cell Stem Cell* 22, 221–234.e8.
- Petreanu, L., and Alvarez-Buylla, A. (2002). Maturation and death of adult-born olfactory bulb granule neurons: role of olfaction. *J. Neurosci.* 22, 6106–6113.
- Piccin, D., Tufford, A., and Morshead, C.M. (2014). Neural stem and progenitor cells in the aged subependyma are activated by the young niche. *Neurobiol. Aging* 35, 1669–1679.
- Pilz, G.-A., Bottes, S., Betizeau, M., Jörg, D.J., Carta, S., Simons, B.D., Helmenchen, F., and Jessberger, S. (2018). Live imaging of neurogenesis in the adult mouse hippocampus. *Science* 359, 658–662.
- Platel, J.-C., Dave, K.A., Gordon, V., Lacar, B., Rubio, M.E., and Bordey, A. (2010). NMDA receptors activated by subventricular zone astrocytic glutamate are critical for neuroblast survival prior to entering a synaptic network. *Neuron* 65, 859–872.
- Ponti, G., Obernier, K., Guinto, C., Jose, L., Bonfanti, L., and Alvarez-Buylla, A. (2013). Cell cycle and lineage progression of neural progenitors in the ventricular-subventricular zones of adult mice. *Proc. Natl. Acad. Sci. USA* 110, E1045–E1054.
- Posada, D., and Buckley, T.R. (2004). Model selection and model averaging in phylogenetics: advantages of akaike information criterion and bayesian approaches over likelihood ratio tests. *Syst. Biol.* 53, 793–808.
- Raue, A., Schilling, M., Bachmann, J., Matteson, A., Schelker, M., Kaschek, D., Hug, S., Kreutz, C., Harms, B.D., Theis, F.J., et al. (2013). Lessons learned from quantitative dynamical modeling in systems biology. *PLoS ONE* 8, e74335.
- Resat, H., Petzold, L., and Pettigrew, M.F. (2009). Kinetic modeling of biological systems. *Methods Mol. Biol.* 541, 311–335.
- Shook, B.A., Manz, D.H., Peters, J.J., Kang, S., and Conover, J.C. (2012). Spatiotemporal changes to the subventricular zone stem cell pool through aging. *J. Neurosci.* 32, 6947–6956.
- Sotiropoulos, V., and Kaznessis, Y.N. (2011). Analytical derivation of moment equations in stochastic chemical kinetics. *Chem. Eng. Sci.* 66, 268–277.
- Stapor, P., Weindl, D., Ballnus, B., Hug, S., Loos, C., Fiedler, A., Krause, S., Hroß, S., Fröhlich, F., Hasenauer, J., and Wren, J. (2018). PESTO: parameter estimation toolbox. *Bioinformatics* 34, 705–707.
- Tropepe, V., Craig, C.G., Morshead, C.M., and van der Kooy, D. (1997). Transforming growth factor- α null and senescent mice show decreased neural progenitor cell proliferation in the forebrain subependyma. *J. Neurosci.* 17, 7850–7859.
- Urbán, N., van den Berg, D.L.C., Forget, A., Andersen, J., Demmers, J.A.A., Hunt, C., Ayrault, O., and Guillemot, F. (2016). Return to quiescence of mouse neural stem cells by degradation of a proactivation protein. *Science* 353, 292–295.
- Yang, J., Plikus, M.V., and Komarova, N.L. (2015). The role of symmetric stem cell divisions in tissue homeostasis. *PLoS Comput. Biol.* 11, e1004629.

STAR★METHODS

KEY RESOURCES TABLE

REAGENT or RESOURCE	SOURCE	IDENTIFIER
Antibodies		
Chicken anti-GFP (1:1,000)	Aves Lab	GFP-1020
Rabbit anti-RFP (1:1,500)	Rockland	600-401-379
Mouse IgG1 anti-GFAP (1:500)	Sigma-Aldrich	G3893
Guinea pig anti-Doublecortin (1:2,000)	Millipore	AB2253
Rabbit anti-Ki67 (1:500)	Leica	6019624
Goat anti-chicken Alexa488 (1:500)	Invitrogen	A11039
Goat anti-rabbit Alexa546 (1:500)	Invitrogen	A11010
Goat anti-rabbit Alexa647 (1:500)	Invitrogen	A31571
Goat anti-rat Alexa647 (1:500)	Invitrogen	A21247
Goat biotinylated anti-guinea pig (1:200)	Vector laboratories	BA-7000
Chemicals, Peptides, and Recombinant Proteins		
Streptavidin-Alexa405 (1:1,000)	Invitrogen	S32351
Normal goat serum	Biozol	S-1000
Tamoxifen	Sigma-Aldrich	T5648-SG
Corn oil	Sigma-Aldrich	08267
Experimental Models: Organisms/Strains		
Mouse	(Calzolari et al., 2015)	GLAST ^{CreERT2} .Confetti
Mouse		Confetti
Software and Algorithms		
MATLAB	this paper	https://github.com/QSCD/NeurogenesisAnalysis
MATLAB: Toolbox CERENA	(Kazeroonian et al., 2016; Stapor et al., 2018)	https://github.com/CERENADevelopers/CERENA/
MATLAB: Toolbox PESTO	(Stapor et al., 2018)	https://github.com/ICB-DCM/PESTO
MATLAB: Toolbox AMICI	(Fröhlich et al., 2016, 2017)	https://github.com/ICB-DCM/AMICI

CONTACT FOR REAGENT AND RESOURCE SHARING

Further information and requests for resources and reagents should be directed to and will be fulfilled by the Lead Contact, Carsten Marr (carsten.marr@helmholtz-muenchen.de).

EXPERIMENTAL MODEL AND SUBJECT DETAILS

Animal handling, breeding and Tamoxifen administration scheme

Mice were housed and handled in accordance with German and European guidelines for the use of animals for research purposes, and experiments were approved by the institutional animal care committee and the government of Upper Bavaria. Mice were housed under standard lighting and temperature control conditions, fed *ad libitum*, in IVC cages provided with carton shelters and Aspen shavings. Both young and aging individuals were maintained in social contact for the whole time preceding labeling; if other experimentally valuable animals were compatible (e.g., littermates, extraneous females) and for as long as social interactions allowed it. Dams were provided with tissues as nesting material. Both males and female adult mice were used for our analyses.

Mouse lines

To conditionally label neural stem cells (NSCs), we used $GLAST^{CreERT2}$, crossed to R26R-Confetti mice, in which a single copy of a Brainbow cassette was inserted into the ubiquitously expressed *Rosa* locus. Tamoxifen-induced Cre activity theoretically results in the random expression of one of four possible fluorescent protein-encoding reporter genes (RFP, YFP, CFP, GFP). However, at low induction doses we could observe the expression of only three reporters. Antibody-based staining allows a clear distinction of all the reporters, based on their distinct intracellular distribution (membrane-tagged CFP, diffuse YFP) or antigenic properties (GFP spectral variants as opposed to RFP).

METHOD DETAILS

1. Experimental methods

1.1 *In vivo* clonal lineage tracing and analysis

In vivo clonal labeling of adult NSCs and tracing of their progeny was performed as previously described by (Calzolari et al., 2015). Briefly, a single dose (10 μ g per g of body weight) of Tamoxifen (Sigma-Aldrich, T5648-SG), dissolved in corn oil (Sigma-Aldrich, 08267) to a final concentration of 1 mg/ml, was administered intra peritoneal/peritoneum to double hemizygous $GLAST^{CreERT2}$:Confetti transgenic mice of 12-14 months of age, of both sexes.

Animals were sacrificed at 21 or 56 days post-labeling (dpl) and were transcardially perfused with a cold solution of 4% paraformaldehyde (wt/vol) dissolved in phosphate-buffered saline (PBS). The dissected brains were postfixed in 4% cold paraformaldehyde for additional 4 hours at 4°C and cut at a thickness of 80 μ m at the microtome (Microtome, HM 650 V). Olfactory bulbs were cut coronally until approximately the elbow of the rostral migratory stream, while more caudally sectioning was performed along sagittal planes. Sections were sequentially collected and, after staining, mounted according to their cutting order. All sections from the hemisphere were analyzed for the expression of the reporter proteins.

The following primary antibodies were used for immunohisto fluorescent stainings: chicken anti-GFP (1:1,000, Aves Lab, GFP-1020), rabbit anti-RFP (1:1,500, Rockland, 600-401-379), mouse IgG1 anti-GFAP (1:500, Sigma-Aldrich, G3893), guinea pig anti-Doublecortin (1:2,000, Millipore, AB2253), rabbit anti-Ki67 (1:500, Leica 6019624). The following fluorophore-labeled secondary antibodies and streptavidin were used: goat anti-chicken Alexa488 (1:500, Invitrogen, A11039), goat anti-rabbit Alexa546 (1:500, Invitrogen, A11010), goat anti-mouse IgG Alexa647 (1:500, Invitrogen, A31571), goat anti-rat IgG Alexa647 (1:500, Invitrogen A21247), and goat biotinylated anti-guinea pig (1:200, Vector laboratories, BA-7000) secondary antibodies and streptavidin-Alexa405 (1:1,000, Invitrogen, S32351). Sections were blocked and permeabilized with 10% (normal goat serum (NGS, vol/vol, Biozol, S-1000) and 0.5% Triton X-100 (vol/vol) while being incubated with the primary antibodies, over two nights, and biotinylated and the secondary antibodies were incubated over one night to optimize staining.

Images were acquired using Zeiss Axioplan and confocal laser scanning microscope (Olympus FV1000). Confocal images were analyzed using Fiji (ImageJ 1.47c).

1.2 Identification of distinct cell types and definition of clones

As previously reported in (Calzolari et al., 2015), sparse NSC labeling allowed defining any group of NSC-derived cells (TAPs, NBs, neurons) sharing Confetti reporter expression in a given hemisphere as a clone.

Cell types in clones were defined on the basis of their antigen expression profile (see Figure 1B). GFAP and DCX were employed to identify astrocytes/NSCs and neuroblasts, respectively. TAPs were recognized as clustered GFAP-, DCX- cells found in the SEZ.

The positions of OB neurons was quantified with Axiovision (Zeiss), on low-magnification snapshots allowing exact neuronal soma position to be measured. Centro-peripheral neuronal position is expressed as the fractional distance along the shortest segment spanning the granule cell layer from the core of the OB.

1.3 Longitudinal population-level data extraction from published sources

Total NSC numbers per hemisphere were obtained from (Calzolari et al., 2015; Shook et al., 2012). Halvened (i.e., per hemisphere) abundances of Lexbright and Lex+/EGFR+ NSCs as reported in (Calzolari et al., 2015) were used as a reference for quiescent and active NSC numbers, under the assumption that the bulk of NSCs (as consistently quantified in (Shook et al., 2012) and (Shook et al., 2012) at P60 at approximately $6 \cdot 10^3$ NSCs per lateral wall) goes unstained under the labeling scheme employed by the authors.

2. Computational methods

The goal of our computational analysis is to infer parameters describing the molecular mechanisms of adult neurogenesis from experimental data, which is available from young and aged adult mice (see Table S1). In particular, we are interested in the division strategies of proliferating cell states (aS, TAP, NB I) and want to identify changes during aging.

The experimentally observed progeny resulting from a single labeled NSC exhibits a noticeable heterogeneity in clone size and clonal composition (see Figure 1A). This suggests that the underlying process is stochastic and cannot be described

fully with a deterministic model. As it has been shown that tissue homeostasis on the cellular level can be accurately described by stochastic models (Gardiner, 2010; Klein and Simons, 2011), we model the process of adult neurogenesis as a Markov process.

Our computational approach is as follows: We describe adult neurogenesis with a reaction system and model the underlying dynamics as a Markov jump process (Fröhlich et al., 2016; Resat et al., 2009) using the Chemical Master Equation (CME) (Gardiner, 2010; Gillespie, 1992). As solving the CME is due to its infinite dimension in general not possible (Resat et al., 2009), we used the link between CME and moment equations (Sotiropoulos and Kaznessis, 2011) and solved the first and second order moment equations (Fröhlich et al., 2016; Resat et al., 2009) instead. The first and second order moments were then used to fit models to the observed data.

We considered four different division strategies for the three proliferating cell states respectively and thereby fitted $4^3 = 64$ different models (see Figure 2A). Based on the Bayesian Information Criterion (Bhat and Kumar, 2010) we compared and ranked the 64 models for both datasets (young and aged) separately (see Figure 2D). We applied model averaging (Link and Barker, 2006) to obtain weighted mean and variance of estimated parameters in young and aged mice. For each model and its corresponding optimal parameters as well as for the average models we were then able to simulate the first and second order moments, but also single clones.

2.1. Model approach

Every cell state is modeled as a compartment (see Figure 2A). According to the transitions between the compartments, we derived all occurring reactions and the respective CME. In the following section, we explain the derivation of the solution of the first and second order moment equations from the CME.

Cell states and model parameters

Let $\mathbf{x} = (dS, qS, aS, T, B_1, B_2, B_3, N)^T$ denote the vector of cell state variables (dormant, quiescent, active neural stem cells, transit-amplifying progenitors, neuroblasts type I, neuroblasts type II, neuroblast type III, and neurons) and

$$\theta = \begin{pmatrix} r_{act1} \\ r_{act2} \\ r_{inact} \\ r_{div} \\ p_{S \rightarrow SS} \\ p_{S \rightarrow TT} \\ p_{T \rightarrow TT} \\ p_{T \rightarrow BB} \\ p_{B_1} \\ p_{B_1 \rightarrow B_1 B_1} \\ p_{B_1 \rightarrow B_2 B_2} \\ r_{mig} \\ p_N \\ p_{dS0} \\ p_{qS0} \end{pmatrix} \quad (1)$$

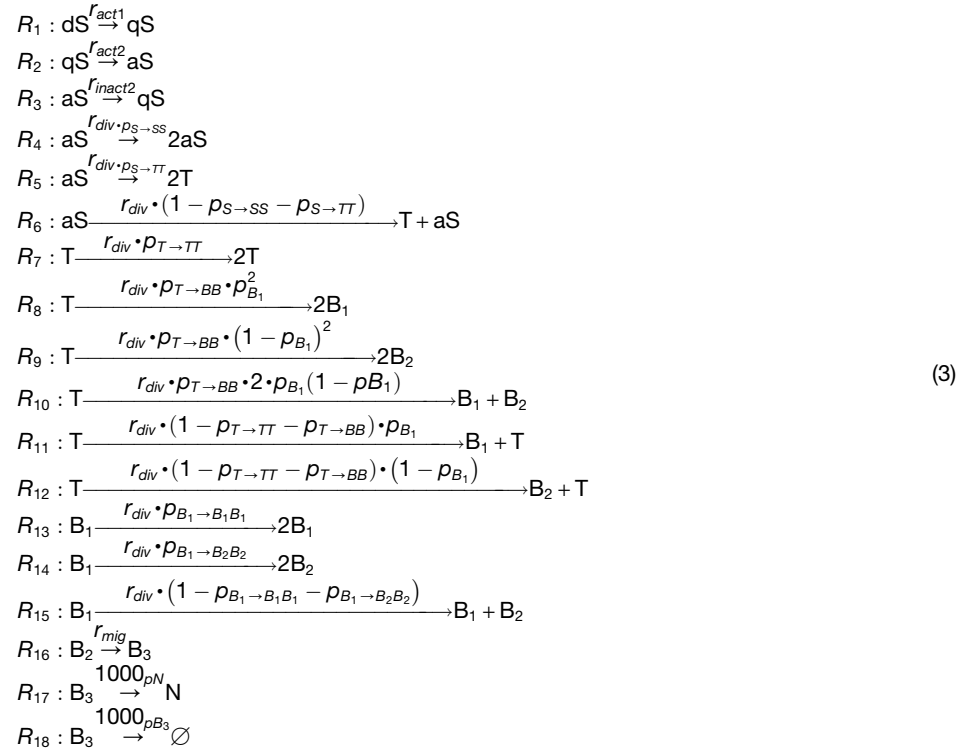
the vector of model parameters, consisting of activation and inactivation rates ($r_{act1}, r_{act2}, r_{inact}$), the division rate (r_{div}), the neuroblast migration (r_{mig}) rate, as well as probabilities of self-renewal ($p_S \rightarrow SS, p_T \rightarrow TT, p_{B_1 \rightarrow B_1 B_1}$), of differentiation ($p_S \rightarrow TT, p_T \rightarrow BB, p_{B_1 \rightarrow B_2 B_2}$), of a TAP differentiating to neuroblast type I (p_{B_1}), of a neuroblast type III to become a neuron p_N and of getting initially labeled (p_{dS0}, p_{qS0}). Note that the remaining probabilities are not part of the parameter vector, but instead defined as complementary probabilities,

$$\begin{aligned} p_{S \rightarrow ST} &= 1 - p_{S \rightarrow SS} = p_{S \rightarrow TT}, \\ p_{T \rightarrow TB} &= 1 - p_{T \rightarrow TT} - p_{T \rightarrow BB}, \\ p_{B_1 \rightarrow B_1 B_2} &= 1 - p_{B_1 \rightarrow B_1 B_1} - p_{B_1 \rightarrow B_2 B_2}, \\ p_{aS0} &= 1 - p_{dS0} - p_{qS0} \text{ and} \\ p_{B_2} &= 1 - p_{B_1}, \\ p_{B_3} &= 1 - p_N, \end{aligned} \quad (2)$$

where p_{B_2} is the probability of a TAP to differentiate to a neuroblast type II and p_{B_3} the probability of a neuroblast type III to die.

Reactions

The reactions of a particular model depend on the division mode of the proliferating cell states (see Figure 2B). For the most general model, all proliferating cell states divide according to the unconstrained (U) division strategy, the $n_r = 17$ reactions are:



Chemical Master Equation (CME)

Let $P(\mathbf{x}|t)$ be the probability to be in a certain state \mathbf{x} , that is to observe a certain number of cells in states $dS, qS, aS, T, B_1, B_2, B_3$ and N , at time t . The CME describes the change of P over time.

For the reactions of the most general model (Equation 3), the CME can be written as

$$\frac{dP(\mathbf{x}|t)}{dt} = \sum_{r=1}^{n_r=18} a_{(r)}(\mathbf{x}-\mathbf{v}_{\cdot,r})P(\mathbf{x}-\mathbf{v}_{\cdot,r}|t) - a_{(r)}(\mathbf{x})P(\mathbf{x}|t), \tag{4}$$

where $\mathbf{v}_{(\cdot,i)}$ indicates the r th column of the stoichiometric matrix

$$\nu = \begin{matrix}
 & R_1 & R_2 & R_3 & R_4 & R_5 & R_6 & R_7 & R_8 & R_9 & R_{10} & R_{11} & R_{12} & R_{13} & R_{14} & R_{15} & R_{16} & R_{17} & R_{18} \\
 dS & -1 & 0 & 0 & 0 & 0 & 0 & 0 & 0 & 0 & 0 & 0 & 0 & 0 & 0 & 0 & 0 & 0 & 0 \\
 qS & 1 & -1 & 1 & 0 & 0 & 0 & 0 & 0 & 0 & 0 & 0 & 0 & 0 & 0 & 0 & 0 & 0 & 0 \\
 aS & 0 & 1 & -1 & 1 & -1 & 0 & 0 & 0 & 0 & 0 & 0 & 0 & 0 & 0 & 0 & 0 & 0 & 0 \\
 T & 0 & 0 & 0 & 0 & 2 & 1 & 1 & -1 & -1 & -1 & 0 & 0 & 0 & 0 & 0 & 0 & 0 & 0 \\
 B_1 & 0 & 0 & 0 & 0 & 0 & 0 & 0 & 2 & 0 & 1 & 1 & 0 & 1 & -1 & 0 & 0 & 0 & 0 \\
 B_2 & 0 & 0 & 0 & 0 & 0 & 0 & 0 & 0 & 2 & 1 & 0 & 1 & 0 & 2 & 1 & -1 & 0 & 0 \\
 B_3 & 0 & 0 & 0 & 0 & 0 & 0 & 0 & 0 & 0 & 0 & 0 & 0 & 0 & 0 & 1 & -1 & -1 & 0 \\
 N & 0 & 0 & 0 & 0 & 0 & 0 & 0 & 0 & 0 & 0 & 0 & 0 & 0 & 0 & 0 & 0 & +1 & 0
 \end{matrix} \tag{5}$$

and $a_{(r)}$ the r th entry of the propensity vector

$$\mathbf{a}(\mathbf{x}) = \begin{bmatrix} r_{act1} \cdot [dS] \\ r_{act2} \cdot [qS] \\ r_{inact} \cdot [aS] \\ r_{div} \cdot \rho_{S \rightarrow SS} \cdot [aS] \\ r_{div} \cdot \rho_{S \rightarrow TT} \cdot [aS] \\ r_{div} \cdot (1 - \rho_{S \rightarrow SS} - \rho_{S \rightarrow TT}) \cdot [aS] \\ r_{div} \cdot \rho_{T \rightarrow TT} \cdot [T] \\ r_{div} \cdot \rho_{T \rightarrow BB} \cdot \rho_{B_1}^2 \cdot [T] \\ r_{div} \cdot \rho_{T \rightarrow BB} \cdot (1 - \rho_{B_1})^2 \cdot [T] \\ r_{div} \cdot \rho_{T \rightarrow BB} \cdot 2 \cdot \rho_{B_1} \cdot (1 - \rho_{B_1}) \cdot [T] \\ r_{div} \cdot (1 - \rho_{T \rightarrow TT} - \rho_{T \rightarrow BB}) \cdot \rho_{B_1} \cdot [T] \\ r_{div} \cdot (1 - \rho_{T \rightarrow TT} - \rho_{T \rightarrow BB}) \cdot (1 - \rho_{B_1}) \cdot [T] \\ r_{div} \cdot \rho_{B_1 \rightarrow B_1 B_1} \cdot [B_1] \\ r_{div} \cdot \rho_{B_1 \rightarrow B_2 B_2} \cdot [B_1] \\ r_{div} \cdot (1 - \rho_{B_1 \rightarrow B_1 B_1} - \rho_{B_1 \rightarrow B_2 B_2}) \cdot [B_1] \\ r_{mig} \cdot [B_2] \\ 1000 \rho_N \cdot [B_3] \\ 1000 \rho_{B_3} \cdot [B_3] \end{bmatrix} \quad (6)$$

Whenever a reaction R_i (for instance R_2 : activation of qS) occurs, the system jumps from a particular state \mathbf{x} , ($\mathbf{x} = ([dS] = 0, [qS] = 1, [aS] = 0, [T] = 0, [NB_1] = 0, [NB_2] = 0, [N] = 0)$) to state $\mathbf{x} + \mathbf{v}_{\cdot i}$ (in this case to state $([dS] = 0, [qS] = 0, [aS] = 1, [T] = 0, [NB_1] = 0, [NB_2] = 0, [N] = 0)$). The CME therefore describes the stochastic evolution of the state vector X_t .

Moment equations

As the solution of the CME is (analytically and numerically) often intractable (Resat et al., 2009), we calculated the first and second order moment equations instead (Equation 8). This is done by using a definition of mean μ_i , variance and covariance C_i of cell state abundances based on the solution of the CME (Engblom, 2006).

$$\begin{aligned} \mu_i(t) &:= E[X_i(t)] = \sum_{x_i} x_i P(\mathbf{x}|t) \\ C_{ij}(t) &:= Cov[X_i(t), X_j(t)] = \sum_{x_i, x_j} (x_i - \mu_i(t))(x_j - \mu_j(t))^T P(\mathbf{x}|t), \end{aligned} \quad (7)$$

with $i, j = 1, 2, \dots, 7$ denoting the cell state index.

We calculated the derivatives to get the evolution equations for the first and second order moment equations:

$$\begin{aligned} \frac{d\mu_i(t)}{dt} &= \sum_{r=1}^{n_r} \nu_{(i,r)} \left(a_{(r)}(\mu(t), \theta) + \frac{1}{2} \sum_{l_1, l_2} \frac{\partial^2 a_{(r)}(\mu(t), \theta)}{\partial x_{l_1} \partial x_{l_2}} C_{l_1, l_2}(t) \right) \\ \frac{dC_{ij}(t)}{dt} &= \sum_{r=1}^{n_r} \left(\nu_{(i,r)} \sum_{l_1} \frac{\partial a_{(r)}(\mu(t), \theta)}{\partial x_{l_1}} C_{l_1, j} + \nu_{(j,r)} \sum_{l_2} \frac{\partial a_{(r)}(\mu(t), \theta)}{\partial x_{l_2}} C_{i, l_2} \right) \\ &+ \sum_{r=1}^{n_r} \nu_{(i,r)} \nu_{(j,r)} \left(a_{(r)}(\mu(t), \theta) + \frac{1}{2} \sum_{l_1, l_2} \frac{\partial^2 a_{(r)}(\mu(t), \theta)}{\partial x_{l_1} \partial x_{l_2}} C_{l_1, l_2}(t) \right). \end{aligned} \quad (8)$$

For any parameter θ , the first and second order moments can be generated by solving the first and second order moment equations (Equation 8). Note that as the reaction propensities are linear in cell states, the moments are closed and application of moment closure is not required.

To solve the ODE system, initial conditions have to be specified according to the experimental setting. In previous work (Calzolari et al., 2015), the probability to label more than one stem cell was calculated to be 0.0024, 0.0115, 0.0696 and 0.2227 at times $t = 3, 7, 21$ and 56 days post labeling for a Tamoxifen dose of $10 \mu g/g$. Accordingly, we assumed for our models that exactly one neural stem cell is labeled at $t_0 = 0$, which can be dormant, quiescent or active according to probabilities p_{dS0} , p_{qS0} and $p_{aS0} = 1 - p_{dS0} - p_{qS0}$. Considering the labeling of a certain NSC state as binomially distributed, we derived the initial first and second order moments

$$\begin{aligned}
 \mu_1(0) &= p_{dS0} \\
 \mu_2(0) &= p_{qS0} \\
 \mu_3(0) &= 1 - p_{dS0} - p_{qS0} \\
 \mu_k(0) &= 0, \quad k = 4, \dots, 8 \\
 C_{1,1}(0) &= p_{dS0}(1 - p_{dS0}) \\
 C_{2,2}(0) &= p_{qS0}(1 - p_{qS0}) \\
 C_{3,3}(0) &= (1 - p_{dS0} - p_{qS0})(p_{dS0} + p_{qS0}) \\
 C_{k,k}(0) &= 0, \quad k = 4, \dots, 8 \\
 C_{1,2}(0) &= C_{2,1}(0) = -\sqrt{p_{dS0} \cdot p_{qS0}} \sqrt{p_{qS0} \cdot p_{dS0}} = -p_{qS0} \cdot p_{dS0} \\
 C_{1,3}(0) &= C_{3,1}(0) = -p_{dS0} \cdot (1 - p_{qS0} - p_{dS0}) \\
 C_{2,3}(0) &= C_{3,2}(0) = -p_{qS0} \cdot (1 - p_{qS0} - p_{dS0}) \\
 C_{k,1}(0) &= 0, \quad k = 4, \dots, 8.
 \end{aligned} \tag{9}$$

2.2 Parameter estimation

Our models contain between 7 and 13 unknown parameters. These parameters are estimated by minimizing the discrepancy between observed and modeled first and second order moments.

Model definition

Let on the one hand $\mathcal{M}(\theta)$ be a particular model consisting of dynamics $\dot{x} = f(x, \theta)$ and model observations $y^{\mathcal{M}} = h(x, \theta)$:

$$\mathcal{M}(\theta) : \left\{ \begin{array}{l} \dot{x} = f(x, \theta) = \left\{ \frac{d\mu_i(t)}{dt}, \frac{dC_{i,j}(t)}{dt} \right\}_{i,j=1,\dots,3}, \quad x_0(\theta) = x_0 \\ y^{\mathcal{M}} = h(x, \theta) = \{ \mu_k(t), C_{k,l}(t) \}_{k,l=1,\dots,3} \end{array} \right\} \tag{10}$$

and let on the other hand $\mathcal{D} = \{t_k, y_j^{\mathcal{D}}(t_k)\}_{k=1}^{n_t}$ be the data we want to fit. Here $y_j^{\mathcal{D}}(t_k)$ denotes the observed moments at time t_k which were directly calculated from clonal observations (see Figure 1A, Table S1). We assumed the observed moments $y_j^{\mathcal{D}}(t_k)$ are subject to additive normally distributed measurement noise (Raue et al., 2013)

$$y_j^{\mathcal{D}}(t_k) = y_j^{\mathcal{M}}(t_k, \theta) + \varepsilon, \text{ with } \varepsilon \sim \mathcal{N}(0, \sigma_{j,k}^2)$$

due to false cell type assignment or counting errors in the clonal data (see Table S1). The variation in experimentally observed moments ($\sigma_{j,k}^2$) was estimated via 1000 bootstraps from the clonal data (see Table S1).

Maximum likelihood estimation

In order to assess how well a particular model fits the experimental data for a certain parameter θ , the log-likelihood $\ell_{\mathcal{D}}(\theta)$ is calculated according to the assumed additive normally distributed measurement noise:

$$\ell_{\mathcal{D}}(\theta) = -\frac{1}{2} \sum_{k=1}^{n_t} \sum_{j=1}^{n_y} \log \left(2\pi\sigma_{j,k}^2 \right) + \left(\frac{(y_j^{\mathcal{D}}(t_k) - y_j^{\mathcal{M}}(t_k, \theta))^2}{\sigma_{j,k}^2} \right), \tag{11}$$

in which n_t is the number of time points and $n_y = 9$ is the number of considered moment equations.

To estimate the unknown parameter vector θ , the optimization problem

$$\begin{aligned}
 \theta^{ML} &= \underset{\theta}{\operatorname{argmax}} \ell_{\mathcal{D}}(\theta), \\
 &\text{subject to } \mathcal{M} \\
 &A\theta \leq b
 \end{aligned} \tag{12}$$

is solved using multi-start local optimization with interior point algorithm (Boyd and Vandenberghe, 2016). The starting values $(\theta^{\text{start}})_i = 1, \dots, 200$ (initial parameter vectors) are determined according to latin hypercube sampling (Eliáš and Vořechovský, 2016). $A \in \mathbb{R}^{p \times m}$ and $b \in \mathbb{R}^p$ define the inequality constraints for θ , which are introduced in the next paragraph.

The resulting optimal parameter is observed at the highest $\ell_{\mathcal{D}}$ value. To ensure that the optimization procedure converged, we checked if this best log-likelihood value is observed several times for different starting values. We observed a plateau of the highest log-likelihood value, indicating the implemented optimization procedure converged.

Assumptions, boundaries and inequality constraints for parameters

To define the optimization problem properly, we need to define biologically meaningful parameter boundaries (see Table S2). We based these on findings of Ponti et al. (2013) for the cell division rate r_{div} and Petreanu and Alvarez-Buylla (2002) for the migration rate r_{BN} . According to the analysis of Ponti et al. (2013) which showed that only 55% of neuroblasts divide, we introduced another neuroblast state and assumed the probability for a TAP to differentiate into the proliferating neuroblast state NB I to be $p_{\text{B1}} = 0.55$. Platel et al. (2010) experimentally determined the percentage of neuroblasts differentiating to neurons to be 78% in

the subependymal zone of P20-P30 mice. We therefore estimate this percentage for the three months- (young) and one year-old (aged) mice by assuming a range of [65,85]% in our model. Moreover, we fitted a stem cell compartment ODE model to cell counts of (Shook et al., 2012) and (Daynac et al., 2016) (see Figure S2A).

This analysis led to two model constraints:

- (i) the dS activation rate was fixed to $r_{act1} = 0.000171$,
- (ii) the difference between qS activation and aS inactivation rates was constrained to $-0.3 \leq r_{inact} - r_{act2} \leq 0.4$.

Another inequality constraint was introduced for division strategy U, in which the sum of probabilities for symmetric self-renewal and symmetric differentiation must be lower or equal to 1. The same holds for the sum of probabilities to initially label a dormant stem cell and to initially label a quiescent stem cell.

2.3. Model selection and averaging

Parameter estimation was performed individually for all $4^3 = 64$ models. These models result from all possible combinations of the four division modes for each of the three proliferating cell states (aS, T, B₁, see Figures 2A–2C). We compared and ranked the 64 different models based on their Bayesian Information Criterion (BIC) value. The BIC is defined as

$$BIC_k : = -2 \log(P(\mathcal{D} | \theta_k^{ML})) + n_{\theta,k} \cdot \log(n_{obs}), \quad (13)$$

where $n_{\theta,k}$ describes the number of parameters of model k and n_{obs} the number of observations used for model fitting (Bhat and Kumar, 2010). Since we could not identify a single best performing model, we applied model averaging (Link and Barker, 2006; Posada and Buckley, 2004). Assuming identical prior probabilities for all models, we approximated the posterior model probability with:

$$P(\mathcal{M}_k | \mathcal{D}) \approx \frac{\exp(-\frac{1}{2} BIC_k)}{\sum_j \exp(-\frac{1}{2} BIC_j)} =: w_k^{BIC} \quad (14)$$

The BIC weights (w_k^{BIC}) were then used to calculate the weighted mean of parameters:

$$\overline{\theta_w^{ML}} = \sum_{k=1}^{64} \theta_w^{ML} \cdot \theta_w^{BIC}, \quad (15)$$

and the standard error of the weighted mean of parameters (Cochran, 2007; Gatz and Smith, 1995) (see Figures 2G, 2H, and S2C–S2E):

$$\begin{aligned} SE_{\overline{\theta_w^{ML}}} = & \frac{64}{(64-1) \left(\sum_{k=1}^{64} w_k^{BIC} \right)} \left(\sum_{k=1}^{64} \left(\theta_w^{ML} \cdot w_k^{BIC} - \overline{w^{BIC}} \cdot \overline{\theta_w^{ML}} \right)^2 \right. \\ & - 2 \cdot \overline{\theta_w^{ML}} \sum_{k=1}^{64} \left(w_k^{BIC} - \overline{w^{BIC}} \right) \left(\theta_w^{ML} \cdot w_k^{BIC} - \overline{w^{BIC}} \cdot \overline{\theta_w^{ML}} \right) \\ & \left. + \overline{\theta_w^{ML}}^2 \sum_{k=1}^{64} \left(w_k^{BIC} - \overline{w^{BIC}} \right)^2 \right). \end{aligned} \quad (16)$$

Resulting division probabilities and BIC values can be found in Table S3.

2.4. Robustness Test

In order to test the robustness of the estimated weighted mean parameter differences between the two groups (young and aged), we repeated the analysis using only the measurements observed at days 21 and 56 for parameter estimation. Resulting probabilities for division strategies can be seen in Figures S2D and S2E.

2.5. Evaluation

As stated in section 2.2, we used recently published data (Shook et al., 2012) to constrain the inactivation and activation rates in our model (see Table S2). From the same analysis, cell counts of subsequent cell-states are available, which we did not include in the parameter estimation. To evaluate if our model is able to describe the cell count dynamics per cell state at the population level, we calculated the first order moment (mean) for each cell state. We set the initial values of our model to the earliest observed measurements and assessed if the model behavior over time agrees with the experimental observations made by Daynac et al. (2016) (Figure 3A).

We performed this analysis based on the average young model (age-independent model) and on an age-dependent model, in which the parameters change with age from the weighted mean parameter in group young ($\overline{\theta_w^{ML}}$) to the weighted mean parameter in group aged ($\overline{\theta_w^{ML,a}}$). We modeled this change in parameters with Hill functions (Figure S3).

The Hill function is defined as

$$H(a, s, n, y_{min}, y_{max}) : = \frac{y_{max} - y_{min}}{(as)^n + 1} + y_{min}, \quad (17)$$

where a denotes the age of mice, n is the Hill coefficient, $1/s$ is the age at which the saddle point of the Hill function is observed and y_{\min} , y_{\max} describe the minimum and maximum values of the Hill function.

We set y_{\min} and y_{\max} to

$$y_{\min} = \min\left(\overline{\theta_{w,y}^{ML}}, \overline{\theta_{w,a}^{ML}}\right)$$

$$y_{\max} = \max\left(\overline{\theta_{w,y}^{ML}}, \overline{\theta_{w,a}^{ML}}\right)$$

and optimized for s and n , assuming the boundaries

$$s \in \left[\frac{1}{t_{aged}}, \frac{1}{t_{young}} \right]$$

and

$$n \in \begin{cases} [1, 10] & , \quad \text{if } \overline{\theta_{w,y}^{ML}} \leq \overline{\theta_{w,a}^{ML}} \\ [-10, -1] & , \quad \text{otherwise.} \end{cases}$$

2.6. Stochastic simulation

We simulated single realizations from the model using the Stochastic Simulation Algorithm (SSA) (Gillespie, 2001) (see Figure 3B). In addition, we simulated individual trees (see Figure 4A), which were used to calculate the percentage of neuron-only clones (see Figure 3D) and genealogical metrics (see Figure 4B). For the simulation of trees, we assumed exponentially distributed (in)activation times and Erlang distributed division and migration times (Figure S4). Resulting mean and median of genealogical metrics are shown in Table S4 for both groups.

In addition, we performed the genealogical metrics estimation assuming exponentially distributed rates. This led to very similar results and all metrics showed the same qualitative behavior.

QUANTIFICATION AND STATISTICAL ANALYSIS

Information regarding the statistical analyses performed on clonal data are indicated in each figure legend. Sample size estimation was not performed. Within each litter, littermates where, whenever present in sufficient numbers, randomly assigned to distinct post-labeling cohorts (21 or 56 days), in balanced numbers.

Computational analyses were performed with MATLAB using the toolboxes PESTO (Stapor et al., 2018) for parameter estimation, CERENA (Kazeroonian et al., 2016) for calculating and solving the first and second order moment equations, and AMICI (Fröhlich et al., 2017) for defining and solving the ODE stem cell compartment model.

Error bars in Figures 1C–1E, S1D, and S1E represent the standard error of the mean values, as calculated across all relevant entities, i.e., the numbers of cells or groups of cells relevant to the various metrics being reported, across all animals for a given experimental group.

The data in Figure 3A show the mean and the standard error of the mean at various time points and were extracted from (Daynac et al., 2016). The error band in Figure 3C as well as the error bars in Figure 3D describe the standard deviation and were estimated for each time point/ group based on model simulations. The calculation of the standard error of the weighted mean (shown in Figures 2G, 2H, and S2C–S2E) is explained in detail in 2.3 (Equation 16).

DATA AND SOFTWARE AVAILABILITY

The experimental data are listed and available in the excel sheets ClonalCompositionData_young.xlsx and ClonalCompositionData_aged.xlsx.

The data (cell counts at 4 different time points for young and aged mice) resulting from the clonal confetti reporter experiment which were used for the computational analysis can be found in Table S1.

The MATLAB code used for the computational analysis is available at <https://github.com/QSCD/NeurogenesisAnalysis>. It includes the code for the stem cell compartment pre-analysis (folder: ODE_StemCellCompartments), toolboxes used for the analysis (folder: Tools) and a main folder for the neurogenesis modeling (folder: NeurogenesisModel). This folder contains a subfolder for model specification, model selection and parameter estimation (subfolder: Modelselection), model validation (subfolder: Evaluation) and SSA and tree simulations (subfolder: Simulation).